LITHOS 406–407 (2021) 106505

Contents lists available at ScienceDirect

LITHOS

journal homepage: www.elsevier.com/locate/lithos

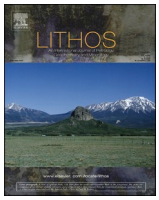

Research Article

Mantle wedge enrichment beneath southern Tibet during the late stage (100–45 Ma) of oceanic subduction: Geochemical constraints from mantle-derived intrusions

Ming Lei [a,b], Jianlin Chen [a,b,*], Fei Huang [a,b], Yixin Liu [a,b]

[a] State Key Laboratory of Isotope Geochemistry, Guangzhou Institute of Geochemistry, Chinese Academy of Sciences, Guangzhou 510640, China
[b] CAS Centre for Excellence in Deep Earth Sciences, Guangzhou 510640, China

ARTICLE INFO

Keywords:
Mantle enrichment
Oceanic sediments
Neo-Tethyan oceanic slab
Lhasa Terrane

ABSTRACT

The Miocene K-rich mafic rocks in the Lhasa Terrane of the southern Tibetan Plateau are considered to be related to either the subduction of the Neo-Tethyan oceanic slab or Indian continental slab. In order to investigate how subduction of the Neo-Tethyan oceanic slab has geochemically affected the mantle beneath southern Tibet, we obtained geochronological and geochemical data for the late Early Cretaceous Cangguo gabbros (97 Ma) and early Eocene Langka diorites (51 Ma) in southern Tibet. Although both the Cangguo gabbros and Langka diorites are characterized by arc-like trace element patterns, with enrichment in light rare earth and large-ion lithophile elements (e.g., Ba, Pb, and U), depletion in high-field-strength elements (e.g., Nb and Ta), and depleted Sr–Nd–Hf isotopic compositions, there are some other major geochemical differences (e.g., Ba/La and Th/La ratios) between these two suites of rocks. These geochemical characteristics of the Cangguo gabbros and Langka diorites indicate they were produced by melting of the depleted mid-ocean ridge mantle (DMM) that was enriched by oceanic sediment-derived fluids and melts, respectively. Our data and previous studies suggest that dehydration and melting of subducted Neo-Tethyan oceanic sediments beneath the Lhasa Terrane occurred in the late stage (100–45 Ma) of Neo-Tethyan oceanic slab subduction, which may have enriched the mantle beneath the Lhasa Terrane. However, the mantle beneath the Lhasa Terrane that was enriched by the subduction of oceanic slab during 100–45 Ma is still isotopically more depleted than the source of Miocene post-collisional K-rich mafic rocks in the Lhasa Terrane. This indicates that the enriched component in the mantle source of the K-rich mafic rocks cannot be simply attributed to materials derived from the Neo-Tethyan oceanic slab, and other additional materials are required.

1. Introduction

Continent–continent collisional orogenic belts are typically associated with the subduction of oceanic lithosphere, closure of oceanic basins, continent–continent collision, and subsequent subduction of continental lithosphere (e.g., Castro et al., 2013; Ernst, 2005). In a typical continent–continent collisional belt, both oceanic and continental crustal materials are recycled into and interact with the overlying mantle (e.g., Zheng and Chen, 2016). In this scenario, the mantle wedge beneath a continent–continent collisional orogen can record crust–mantle interactions in both the continental and earlier oceanic subduction channels (e.g., Zheng and Chen, 2016). The southern Tibetan Plateau is a typical continent–continent collisional orogeny, and records subduction of Neo-Tethyan oceanic and Indian continental lithosphere (e.g., Chung et al., 2005). The Miocene (24–8 Ma) post-collisional K-rich (ultrapotassic–potassic) mafic rocks are widely distributed in the Lhasa Terrane and are unique mantle-derived magmas produced after the collision between India and Asia. These K-rich mafic rocks have arc-like trace element patterns and highly enriched Sr − Nd isotopic compositions (e.g., Turner et al., 1996; Miller et al., 1999; Ding et al., 2003; Gao et al., 2007; Guo et al., 2013; Liu et al., 2015). However, because the mantle wedge beneath the Lhasa Terrane might have been affected by two different episodes of subduction (i.e., the northward subduction of the Neo-Tethyan oceanic slab and subsequent indentation of the Indian continental lithosphere), it is still unclear how this isotopically enriched mantle source formed. For example, some studies have proposed that

* Corresponding author.
E-mail address: lzdxchen@gig.ac.cn (J. Chen).

https://doi.org/10.1016/j.lithos.2021.106505
Received 17 May 2021; Received in revised form 14 October 2021; Accepted 17 October 2021
Available online 22 October 2021

this isotopically enriched mantle formed by the subduction of Indian continental crust (e.g., Ding et al., 2003; Guo et al., 2013), whereas other studies have proposed it resulted from introduction of oceanic slab-derived materials during Neo-Tethyan subduction (Gao et al., 2007; Liu et al., 2015; Tommasini et al., 2010). Thus, understanding the relationship between the subduction of the Neo-Tethyan oceanic slab and its geochemical effects on the mantle beneath the Lhasa Terrane is the key to resolving this controversy. In general, a subducted oceanic slab consists of oceanic crust and overlying sediments, and there are trace element and isotopic differences between these two components (Chauvel et al., 2009; Plank, 2014; Vervoort et al., 1999, 2011). Previous studies have demonstrated that both oceanic crust and overlying sediments can derive aqueous fluids and/or melts that can enrich the mantle wedge (Carpentier et al., 2009; Labanieh et al., 2010). However, the nature of enrichment in a particular subduction system depends mainly on its thermal structure (Watt et al., 2013). For example, slab-derived fluid-mediated enrichment has prevailed in relatively cold subduction zones, such as the Izu–Bonin–Mariana arcs (e.g., Hauff et al., 2003). In contrast, sediment-derived, melt-mediated enrichment is dominant in relatively hot subduction zones, including the Lesser Antilles and Banda arcs (e.g., Labanieh et al., 2010; Nebel et al., 2011).

It has previously been proposed that initial northward subduction of the Neo-Tethyan oceanic slab might have occurred in the Late Triassic–Early Jurassic (210–174 Ma; Zhu et al., 2008, 2011; Ji et al., 2009; Kang et al., 2014). Subsequently, the initial collision of India and Asia occurred during 65–55 Ma (e.g., Hu et al., 2016; Zhu et al., 2015). During the initial collision of India and Asia, the oceanic slab continued to subduct and dehydrate, thereby producing fluids and melts, which resulted in normal continental arc magmatism and enrichment of the overlying mantle (e.g., Huang et al., 2019, 2020; Zhu et al., 2015). Previous studies have argued that the termination of oceanic slab subduction finally occurs when the slab pull force disappears (e.g., slab break-off; Davies and von Blanckenburg, 1995). Hence, slab break-off of Neo-Tethyan oceanic crust might record the termination of oceanic subduction in the mantle beneath southern Tibet, which occurred during 53–45 Ma (e.g., Ji et al., 2009, 2016; Leech et al., 2005; Zhu et al., 2013, 2015). Therefore, Mesozoic–Cenozoic (210–45 Ma) mantle-derived rocks in the Lhasa Terrane are suitable for investigating the geochemical effects from Neo-Tethyan oceanic slab subduction on the mantle beneath the Lhasa Terrane. Most studies have focused on Late Triassic–Early Jurassic mafic rocks (e.g., Late Triassic Quxu gabbros, Jurassic Yeba Formation, and Sangri Group) in the Lhasa Terrane, and concluded that oceanic crust-derived, fluid-mediated enrichment was predominant at this time. As such, these mafic rocks tend to have nearly mid-ocean ridge basalt (MORB)-like depleted Sr − Nd − Hf isotopic compositions, and high Ba/La and low Th/Nd ratios (e.g., Kang et al., 2014; Meng et al., 2015; Zhu et al., 2008). However, it is unclear how the mantle beneath the Lhasa Terrane was geochemically modified during the Late Cretaceous–early Eocene (100–45 Ma) by Neo-Tethyan oceanic slab subduction, mainly due to the rarity of exposed mantle-derived rocks during this time. This study presents the detailed petrological, geochronological, major and trace element, and Sr–Nd–Hf isotopic data for two mantle-derived intrusions generated in the late stage (100–45 Ma) of Neo-Tethyan oceanic slab subduction in the Lhasa Terrane. We use our data, along with those from previous studies, to: (1) constrain the source and petrogenesis of these rocks; (2) assess how the mantle source was geochemically modified by subduction of the oceanic slab; (3) explore how the enriched source of the post-collisional K-rich mafic rocks formed.

2. Geology of the study area and sampling

The Tibetan Plateau consists of the Songpan–Gangzi, Qiangtang, Lhasa, and Himalaya Terranes from north to south. The Lhasa Terrane is bounded by the Bangong–Nujiang suture zone (BNSZ) to the north and the Indus–Yarlung Zangbo suture zone (IYZSZ) to the south (Fig. 1a). It is generally accepted that BNSZ marks the closure of the Bangong–Nujiang Ocean during the Late Cretaceous to Early Cretaceous,

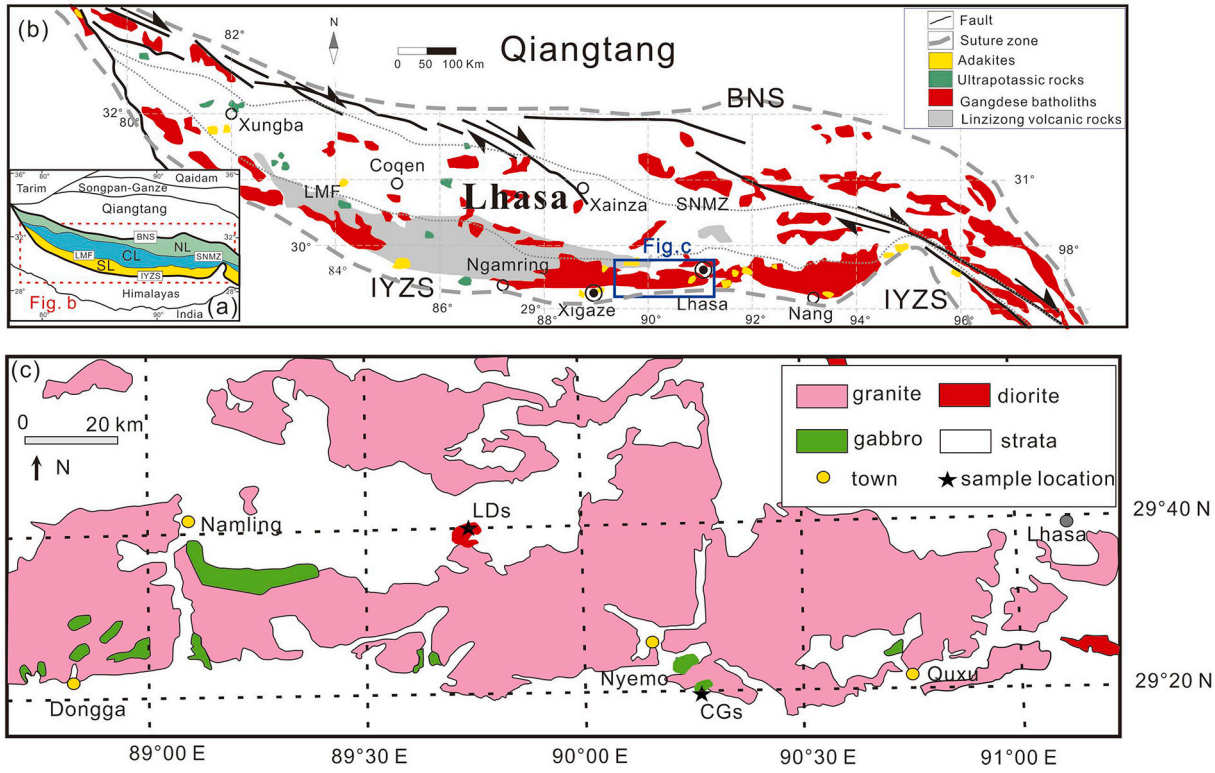

Fig. 1. (a) The Lhasa Terrane in the context of the Tibetan Plateau. (b) Geological map of the Lhasa Terrane, modified from Huang et al. (2019). (c) Simplified map of sample locations in the Lhasa Terrane. Abbreviations: BNS = Bangong–Nujiang Suture; IYZS = Indus–Yarlung Zabong Suture.

whereas the IYZSZ marks the closure of the Neo-Tethyan Ocean during the Late Cretaceous to Early Paleogene (Dewey et al., 1988; Yin and Harrison, 2000). The Lhasa Terrane could be subdivided into the northern, central, and southern subterranes separated by the Shiquan River–Nam Tso Mélange zone (SNMZ) and Luobadui–Milashan fault (LMF), respectively (Fig. 1b, Zhu et al., 2011).

The northern Lhasa subterrane is dominated by juvenile crust covered by the Middle Triassic to Cretaceous sedimentary rocks along with Early Cretaceous volcanic rocks (andesite, dacite, rhyolite, and volcaniclastic rocks) and associated granitoids (Zhu et al., 2011, 2013). The central Lhasa subterrane is commonly considered as an ancient microcontinent with Precambrian basement rocks (Zhu et al., 2011, 2013). The Precambrian basement was covered with Ordovician, Silurian, Permian-Carboniferous, Triassic, and Late Jurassic-Early Cretaceous volcano-sedimentary rocks (Zhu et al., 2011, 2013). The early Cretaceous magmatic rocks in this subterrane were extending ~1200 km and yielded ages of 140–100 Ma (Zhu et al., 2011). The southern Lhasa subterrane may represent the southernmost part of the Asian lithosphere. The southern Lhasa subterrane is considered to be the juvenile continental crust dominated by the Late Triassic to Eocene (205–40 Ma) Gangdese batholith (Chung et al., 2005; Ji et al., 2009), the Mesozoic Yeba Formation, the Sangri Group, the Paleogene Linzizong volcanic succession, and post-collisional (ultra)potassic and adakitic rocks (Chung et al., 2005; Ji et al., 2009; Mo et al., 2007, 2008). Both the Cangguo gabbros and Langka diorites were sampled in the central part of southern Lhasa subterrane (Fig. 1b).

The Cangguo gabbros (CGs) are located in the Cangguo county, 10 km southeast of Nyemo town (Fig. 1c). The gabbros are dark gray, fine- to medium-grained, and consist of hornblende, plagioclase, clinopyroxene with accessory zircon and apatite (Fig. 2a–b).

The Langka diorites (LDs) lie in the Langka county, 70 km northwest of Nyemo town (Fig. 1c). These rocks are medium- to coarse-grained and mainly consist of hornblende, plagioclase, and biotite along with accessory Fe—Ti oxides (Fig. 2c–d).

3. Analytical techniques

3.1. Zircon U-Pb dating

Zircons were extracted from fresh samples following normal separation methods, and they were then handpicked and mounted together onto double-sided adhesive tape before being enclosed in epoxy resin discs. Zircon U-Pb analyses of samples 19CG–08 and 19LK–07 were conducted in an Agilent 7700e ICP-MS system equipped with a 193 nm laser, at Sample Solution Analytical Technology Co., Ltd. (Wuhan, China). The zircon 91,500 was used as the external standard, and NIST SRM 610 were used as the reference material. The detailed analytical technique has been outlined by Zong et al. (2017). The time-resolved spectra were analyzed off-line by ICPMSDataCal software. The common-Pb correction followed the method described by Andersen (2002). The Isoplot/Ex 3.0 software (Ludwig, 2003) was used for calculating U-Pb ages.

3.2. Whole-rock major and trace element analyses

All samples were crushed to select fresh chips. The whole-rock major, trace element and Sr–Nd–Hf isotope analyses were also determined at Sample Solution Analytical Technology Co., Ltd. (Wuhan, China). The fresh chips were powdered in an agate mill to 200 mesh. Whole-rock major and trace element analyses were determined by X-ray fluorescence (XRF) spectrometry and inductively coupled plasma mass spectrometry (ICP-MS), respectively. For major elements, the analytical

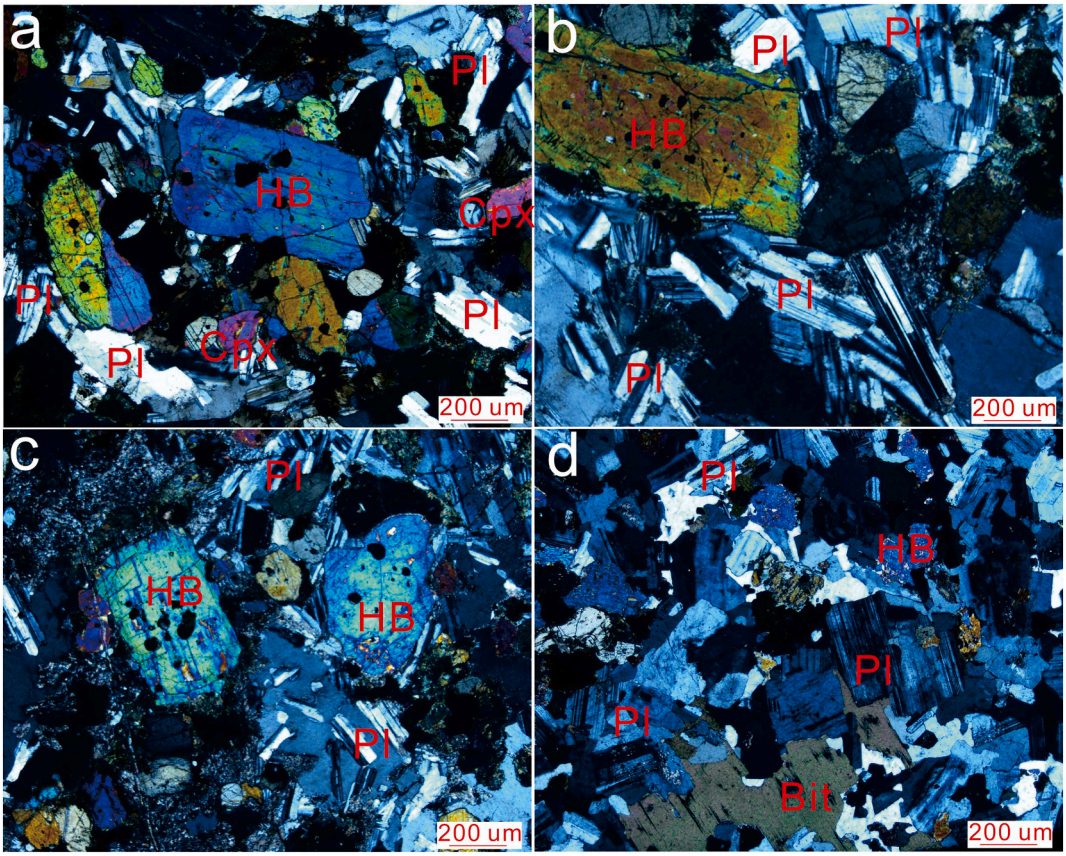

Fig. 2. Photomicrographs of the CGs and LDs. (a) and (b) clinopyroxene, hornblende and plagioclase phenocrysts from the CGs. (c) and (d) hornblende, plagioclase, and biotite phenocrysts from the LDs. Abbreviations here: Cpx, clinopyroxene; Pl, plagioclase; Hb, hornblende; Bit, biotite.

errors are within 5%. Precision for trace elements is better than 10%, based on repeated analysis of USGS standards AGV-2, BCR-2 and BHVO-2. The measured values for rock standards are provided in Supplementary table 1.

3.3. Sr–Nd–Hf isotope analyses

The Sr–Nd–Hf isotopes were measured using a Thermo-Fisher Neptune multicollector ICP-MS system. For the Sr-Nd isotopic analysis, whole powders were dissolved in HF–$HClO_4$ and the dissolution was conducted at 200 °C for one week. Sr and Nd were separated using conventional ion exchange columns, and the Nd fractions were further separated with HDEHP columns. The measured $^{87}Sr/^{86}Sr$ and $^{143}Nd/^{144}Nd$ ratios were normalized to $^{86}Sr/^{88}Sr = 0.1194$ and $^{146}Nd/^{144}Nd = 0.7219$, respectively. The reported $^{87}Sr/^{86}Sr$ and $^{143}Nd/^{144}Nd$ ratios were adjusted to the NBS SRM 987 standard ($^{87}Sr/^{86}Sr = 0.710241 \pm 12$, 2σ, $n = 8$) and the JNdi-1 standard ($^{143}Nd/^{144}Nd = 0.512115 \pm 7$, 2σ, n = 8), respectively. The procedural blanks were 200 pg for Sr and ~ 30 pg for Nd. For the Hf isotopic analysis, about 200 mg of powders were digested in Teflon bombs with a mixture of concentrated HNO_3 + HF and dried on a hot plate. This was followed by the addition of concentrated HNO_3, HF and $HClO_4$ sealed in bombs and kept in an oven at 190 °C. After cooling, the Teflon bomb was opened and then 1 ml HNO_3 was added and evaporated to dryness. A modified ion exchange single-column of LN-Spec resin was used for Hf separation. Mass discrimination correction was carried out via internal normalization to $^{179}Hf/^{177}Hf$ ratio of 0.7325. During our analysis, replicate measurements of the Hf standard JMC 475 gave $^{176}Hf/^{177}Hf$ of 0.282152 ± 0.000010 (2σ, $n = 3$). In-house Alfa Hf standard measured during analysis gave an average $^{176}Hf/^{177}Hf$ of 0.282224 ± 0.000015 (2σ, $n = 10$). The procedural blank was 50 pg for Hf. Isotope ratios of geological reference materials (BCR-2, RGM) measured during the

Table 1
Whole- rock major and trace elements of Cangguo gabbros (CGs) and Langka diorites (LDs).

Sample	19CG-01	19CG-02	19CG-03	19CG-04	19CG-05	19CG-06	19CG-07	19CG-08	19LK-01	19LK-02	19LK-03	19LK-03a	19LK-04	19LK-05	19LK-06	19LK-07
(wt%)																
SiO_2	49.32	48.91	49.30	49.41	49.23	48.07	49.55	49.00	60.75	60.79	58.83	58.90	61.10	61.04	60.51	58.59
TiO_2	0.88	0.88	0.88	0.83	0.85	0.90	0.84	0.87	0.79	0.78	0.81	0.80	0.79	0.77	0.78	0.83
Al_2O_3	17.26	16.77	16.49	17.00	16.90	16.49	17.01	16.61	16.01	16.00	16.54	16.48	16.28	16.11	16.10	16.56
TFe_2O_3	10.69	10.70	10.50	10.24	10.37	10.96	10.11	10.40	6.71	6.64	7.27	7.29	6.48	6.43	6.70	7.41
MnO	0.19	0.20	0.19	0.19	0.19	0.20	0.19	0.20	0.11	0.11	0.13	0.13	0.11	0.11	0.11	0.13
MgO	5.05	5.02	5.23	5.00	5.13	5.48	4.89	5.34	2.96	2.91	3.22	3.21	2.71	2.80	2.97	3.24
CaO	10.67	10.69	10.73	10.43	10.47	11.26	10.13	10.88	5.28	5.26	5.95	5.98	5.47	5.24	5.43	5.99
Na_2O	2.72	2.71	2.59	2.76	2.93	2.56	2.70	2.90	3.43	3.47	3.67	3.70	3.67	3.50	3.49	3.66
K_2O	2.43	2.53	2.56	2.78	2.39	2.01	2.96	1.99	3.09	3.07	2.36	2.40	2.49	3.06	2.90	2.42
P_2O_5	0.42	0.48	0.45	0.47	0.46	0.53	0.43	0.45	0.20	0.19	0.22	0.21	0.21	0.19	0.20	0.21
Mg#	52.4	52.2	53.7	53.2	53.5	53.8	53.0	54.5	50.7	50.6	50.8	50.7	49.4	50.4	50.8	50.5
LOI	0.08	0.42	0.65	0.30	0.52	0.91	0.56	0.81	0.44	0.33	0.62	0.55	0.53	0.40	0.40	0.49
total	99.69	99.32	99.57	99.37	99.45	99.38	99.35	99.44	99.75	99.54	99.61	99.64	99.84	99.64	99.59	99.51
Li	6.66	13.7	9.57	9.10	14.6	16.8	12.3	8.57	20.4	18.1	19.2		20.0	18.2	19.2	19.2
Be	0.90	1.15	1.07	1.50	1.26	1.05	1.25	1.11	1.45	1.54	1.48		1.78	1.59	1.37	1.64
Sc	24.2	25.1	25.8	24.7	24.8	27.5	23.5	26.2	15.5	15.6	17.8		14.9	14.7	15.6	18.0
V	314	319	318	308	318	334	302	315	142	144	159		137	136	142	161
Cr	19.3	17.6	28.7	18.9	18.6	23.4	20.2	27.8	27.5	28.8	30.5		22.2	25.3	29.2	31.8
Co	34.5	35.5	36.5	33.8	37.0	38.8	32.5	34.9	19.6	19.8	21.6		18.8	18.5	19.8	21.8
Ni	22.2	22.9	22.5	21.3	23.1	23.9	21.4	23.9	17.4	17.9	19.6		14.9	16.2	17.2	19.5
Cu	128	169	146	142	117	167	87.6	89.9	44.5	49.5	47.3		52.8	44.6	48.4	41.5
Zn	83.0	89.6	84.6	84.5	85.4	91.7	83.9	83.6	74.9	74.2	77.1		73.4	68.1	70.1	78.2
Ga	17.8	18.4	17.4	18.1	18.2	18.1	17.9	18.1	17.8	18.0	18.7		19.2	17.7	17.8	18.2
Rb	36.3	44.1	39.6	48.0	53.2	30.0	51.0	34.2	107	107	84.2		96.5	103	97.8	83.7
Sr	1268	1231	1185	1205	1224	1178	1250	1154	472	481	526		473	473	482	526
Y	19.9	23.5	21.7	22.5	21.2	23.4	21.0	22.2	23.2	23.8	24.0		25.7	22.9	23.1	24.3
Zr	39.9	55.8	39.6	55.6	37.6	48.4	57.7	41.8	177	178	144		187	176	154	137
Nb	1.49	2.46	1.26	2.43	1.78	1.48	2.35	1.53	8.52	9.10	7.89		9.35	8.21	8.19	9.02
Sn	0.66	0.75	0.70	0.73	0.73	0.76	0.72	0.76	1.38	1.36	1.34		1.53	1.32	1.28	1.30
Cs	0.80	2.39	1.00	2.36	1.24	1.36	1.90	0.66	8.28	7.91	5.85		5.81	7.82	7.28	6.32
Ba	1153	1194	1316	1276	1181	984	1390	1020	602	606	548		450	596	595	561
La	20.4	23.7	21.6	23.1	22.2	24.0	21.9	21.1	22.9	23.5	23.2		26.3	22.8	22.6	22.7
Ce	40.1	48.3	43.1	46.3	44.2	48.8	44.3	43.2	47.5	48.8	48.2		55.5	47.1	46.9	47.7
Pr	5.01	5.97	5.47	5.74	5.41	6.15	5.46	5.52	5.76	5.88	5.87		6.71	5.69	5.71	5.95
Nd	21.6	25.2	23.8	24.1	22.8	26.5	23.5	23.5	22.7	22.8	23.0		26.0	22.2	22.1	23.5
Sm	5.23	6.01	5.65	5.83	5.62	6.30	5.71	5.92	4.92	5.10	5.07		5.38	4.73	4.38	4.92
Eu	1.90	1.93	1.82	2.05	1.87	1.90	1.87	1.92	1.11	1.09	1.22		1.14	1.07	1.10	1.23
Gd	4.69	5.55	5.02	5.16	4.84	5.69	4.82	5.30	4.00	4.13	4.38		4.54	4.00	3.97	4.49
Tb	0.67	0.82	0.75	0.70	0.70	0.85	0.74	0.73	0.65	0.68	0.69		0.73	0.61	0.67	0.73
Dy	3.71	4.06	4.00	3.94	3.76	4.30	3.88	4.10	3.88	3.97	4.02		4.31	3.82	3.95	4.29
Ho	0.70	0.80	0.79	0.80	0.71	0.84	0.73	0.75	0.81	0.81	0.82		0.88	0.78	0.77	0.85
Er	1.86	2.16	1.99	2.07	1.99	2.24	1.99	2.07	2.29	2.31	2.35		2.53	2.23	2.21	2.43
Tm	0.24	0.29	0.27	0.28	0.26	0.29	0.27	0.27	0.32	0.34	0.33		0.37	0.33	0.33	0.35
Yb	1.59	1.82	1.71	1.73	1.65	1.83	1.65	1.79	2.23	2.24	2.27		2.46	2.16	2.13	2.37
Lu	0.23	0.27	0.24	0.25	0.24	0.27	0.25	0.25	0.33	0.34	0.34		0.37	0.33	0.32	0.35
Hf	1.29	1.72	1.41	1.55	1.18	1.52	1.60	1.38	4.68	4.81	4.00		5.29	4.61	4.31	3.97
Ta	0.082	0.12	0.084	0.14	0.11	0.091	0.12	0.082	0.61	0.65	0.59		0.70	0.64	0.59	0.66
Tl	0.033	0.058	0.064	0.045	0.13	0.036	0.072	0.058	0.51	0.48	0.36		0.42	0.43	0.40	0.35
Pb	6.43	7.09	6.44	8.42	6.47	7.03	7.45	6.26	17.9	18.3	17.5		16.4	18.6	18.0	17.8
Th	1.04	2.28	0.95	2.69	1.47	1.13	2.58	1.19	12.5	10.5	13.4		15.6	12.9	8.44	11.0
U	0.29	0.64	0.41	0.78	0.53	0.31	0.73	0.56	3.00	3.63	2.76		3.58	3.87	3.33	2.91

Note: Total iron as TFe_2O_3; Mg# = 100 × Mg^{2+} / (Mg^{2+} + Fe^{2+}), assuming Fe^{3+} / (Fe^{2+} + Fe^{3+}) = 0.15. LOI = loss on ignition.

analytical procedure are presented in Supplementary table 2.

4. Results

The LA-ICPMS zircon U-Pb geochronology data for the CGs and LDs are given in Supplementary table 3. Whole rock major- trace element and Sr–Nd–Hf isotope data for the CGs and LDs are listed in Table 1 and Table 2, respectively.

4.1. Zircon U-Pb ages

Representative CL images of analyzed zircon and U-Pb concordia diagrams of two samples are shown in Fig. 3. The zircon grains from CGs and LDs are euhedral to subhedral, and show oscillatory zoning in CL images, and have high Th/U values (typically >0.1; Fig. 3; Supplementary table 3), indicating an igneous origin. Therefore, the U-Pb zircon ages represent the timing of crystallization of these magmatic rocks. Zircon grains from one sample of CGs (19CG–08) yield weighted-mean $^{206}Pb/^{238}U$ ages of 97.1 ± 0.2 Ma (MSWD = 0.49) (Fig. 3a). Zircon grains from one sample of LDs (19LK–07) yield weighted-mean $^{206}Pb/^{238}U$ ages of 50.9 ± 0.4 Ma (MSWD = 1.02) (Fig. 3b).

4.2. Whole-rock major- trace elements and Sr–Nd–Hf isotopes

The CGs have relatively homogeneous MgO (4.89–5.48 wt%), $Mg^{\#}$ (52.2–54.5), Ni (21.3–23.9 ppm), K_2O (1.99–2.96 wt%), and SiO_2 (48.1–49.6 wt%) values with high K_2O/Na_2O ratios (0.69–1.1), belonging to the shoshonite series (Fig. 4). The CGs show enrichment of light rare earth elements (LREEs), large ion lithophile elements (LILEs; e.g., Ba, U, Pb, and Sr) and depletion in high field strength elements (HFSEs; e.g., Nb, Ta, Zr, and Hf) on the chondrite-normalized REE and primitive mantle-normalized multi-elements variation diagrams (Fig. 5). Compared with CGs, the LDs have obviously lower MgO (2.71–3.24 wt%), $Mg^{\#}$ (49.4–50.8), Ni (14.9–19.6 ppm), higher SiO_2 (58.6–61.1 wt%), and K_2O (2.36–3.09 wt%) values with slightly lower K_2O/Na_2O (0.65–0.90) ratios, which belong to the high-K calc-alkaline series (Figs. 4). The LDs show enrichment of LREEs with high $(La/Yb)_N$ values (6.9–7.7) (Fig. 5a) and are characterized by enrichment of Pb, Th, U, and depletion of Nb and Ti on primitive mantle-normalized multi-elements variation diagram (Fig. 5b).

The CGs are characterized by the lower initial $^{87}Sr/^{86}Sr_{(i)}$ ratios (0.703754–0.703796), higher $\varepsilon Nd_{(t)}$ (+3.5 to +3.8), and $\varepsilon Hf_{(t)}$ values (+11.5 to +12.5) than those of the LDs ($^{87}Sr/^{86}Sr_{(i)}$ = 0.704295–0.704340; $\varepsilon Nd_{(t)}$ = +2.8 − +3.0; $\varepsilon Hf_{(t)}$ = +9.3 − +10.1) (Fig. 6). Both of them have positive $\Delta\varepsilon Hf_{(t)}$ (+3.3 − +4.5 for CGs and + 2.2 − +3.1 for LDs, $\Delta\varepsilon Hf_{(t)} = \varepsilon Hf_{(t)} - 1.36\varepsilon Nd_{(t)} - 2.89$, Vervoort et al., 1999) and plot above the terrestrial array in an Nd-Hf isotopic space (Fig. 6b).

5. Discussion

5.1. Effects of crustal contamination and fractional crystallization

To constrain the nature of the mantle source of the studied rocks, we first assessed the possible effects, if any, due to low-pressure processes such as crustal contamination and fractional crystallization (FC). Based on the following lines of evidence, we suggest that crustal contamination was insignificant. Firstly, no zircon xenocrysts were found in the studied rocks. Secondly, both the CGs and LDs exhibit limited variations in $^{87}Sr/^{86}Sr_{(i)}$ ratios and $\varepsilon Nd_{(t)}$ values with decreasing MgO contents (Fig. 7a–b). Thirdly, given that CGs and LDs were sampled in the southern Lhasa subterrane which was proven to be the juvenile continental crust with depleted Sr-Nd isotopic values and low Nb/La ratios (e.g., Rudnick and Gao, 2003; Zhu et al., 2013), mantle-derived magmas contaminated by such crustal materials will exhibit decreasing Nb/La with decreasing $^{87}Sr/^{86}Sr_{(i)}$ and increasing $\varepsilon Nd_{(t)}$. However, $^{87}Sr/^{86}Sr_{(i)}$ ratios and $\varepsilon Nd_{(t)}$ values of the studied samples do not correlate with Nb/La ratios (Fig. 7c–d), thereby ruling out significant crustal contamination.

Compared with primitive mantle-derived magmas, which have high Ni contents (400 ppm) and $Mg^{\#}$ (73–81) values (Wilson, 1989), the low $Mg^{\#}$ values (52.2–54.5 for the CGs; 49.4–50.8 for the LDs) and Ni concentrations (21.3–23.9 ppm for the CGs; 14.9–19.6 ppm for the LDs) of the CGs and LDs suggest their parental magmas have undergone some FC. The positive correlations between Ni, CaO, and MgO contents suggest that the CGs experienced FC of olivine and clinopyroxene (Fig. 8a–b). The lack of positive correlations between Al_2O_3, Sr, and MgO contents indicate that plagioclase fractionation was insignificant (Fig. 8c–d). However, fractionation of plagioclase and hornblende appears to have dominated the evolution of the LDs magmas, as evidenced by the positive correlations between Al_2O_3, Sr, TFe_2O_3, Sc, and MgO contents (Fig. 8c–f). This is consistent with the presence of plagioclase and hornblende phenocrysts in the LDs.

Given that crustal contamination was negligible during the generation of the CGs and LDs, the geochemical variations in the two intrusions were largely due to crystal fractionation. Although FC of some minerals (olivine, pyroxene, plagioclase, and hornblende) would cause variations in whole-rock major element (e.g., MgO, Al_2O_3, and CaO) and trace element (e.g., Sr) contents, this process would not significantly affect the ratios of some incompatible trace elements, such as Ba/ La, Th/Sm, and Th/La (e.g., Singer et al., 2007). In the following section, these trace element ratios and Sr–Nd–Hf isotope data for the CGs and LDs are used to constrain the nature of their mantle source.

5.2. Mantle source

5.2.1. Mantle source of the CGs

The CGs were produced in the Gangdese continental arc setting, and

Table 2
Whole- rock Sr-Nd-Hf isotope for Cangguo gabbros (CGs) and Langka diorites (LDs).

Sample	19CG-01	19CG-02	19CG-03	19CG-04	19CG-05	19LK-01	19LK-02	19LK-03	19LK-04	19LK-05
$^{87}Sr/^{86}Sr$	0.703878	0.703905	0.703925	0.703907	0.703946	0.704770	0.704753	0.704638	0.704753	0.704736
2σ	0.000010	0.000008	0.000011	0.000010	0.000010	0.000013	0.000009	0.000009	0.000008	0.000012
$^{143}Nd/^{144}Nd$	0.512801	0.512796	0.512799	0.512795	0.512791	0.512768	0.512771	0.512762	0.512757	0.512770
2σ	0.000004	0.000004	0.000003	0.000004	0.000004	0.000003	0.000004	0.000006	0.000004	0.000004
$^{176}Hf/^{177}Hf$	0.283106	0.283104	0.283088	0.283080	0.283086	0.283034	0.283022	0.283014	0.283025	0.283012
2σ	0.000007	0.000007	0.000008	0.000007	0.000006	0.000006	0.000006	0.000008	0.000009	0.000008
$^{87}Sr/^{86}Sr_{(i)}$	0.703768	0.703767	0.703796	0.703754	0.703779	0.704312	0.704304	0.704314	0.704340	0.704295
$\varepsilon Nd_{(t)}$	3.8	3.7	3.8	3.7	3.5	2.9	3.0	2.8	2.8	3.0
$\varepsilon Hf_{(t)}$	12.4	12.5	11.8	11.6	11.5	10.1	9.6	9.3	9.7	9.3
$\Delta\varepsilon Hf_{(t)}$	4.3	4.5	3.7	3.7	3.7	3.1	2.6	2.5	3.0	2.2

Note: The initial Sr–Nd–Hf isotopic values of studied rocks were calculated using their eruption ages. The present chondrite has: $^{87}Rb/^{86}Sr = 0.0847$; $^{87}Sr/^{86}Sr = 0.7045$; $^{147}Sm/^{144}Nd = 0.1967$, $^{143}Nd/^{144}Nd = 0.512638$, $^{176}Lu/^{177}Hf = 0.0332$, and $^{176}Hf/^{177}Hf = 0.282772$. $\Delta\varepsilon Hf_{(t)} = \varepsilon Hf_{(t)} - 1.36\varepsilon Nd_{(t)} - 2.89$ (Vervoort et al., 1999).

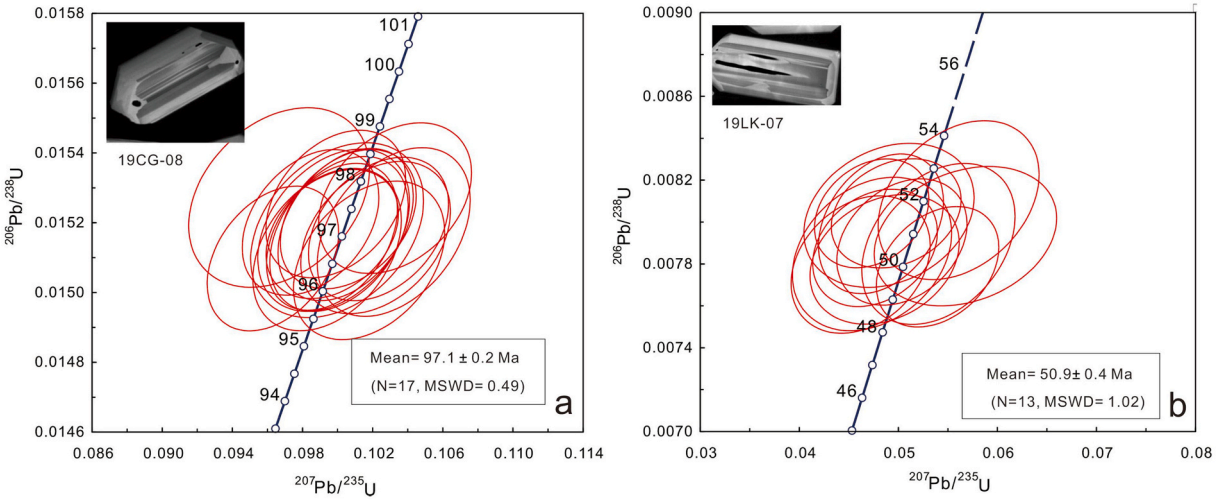

Fig. 3. Zircon U—Pb Concordia diagrams of the CGs and LDs.

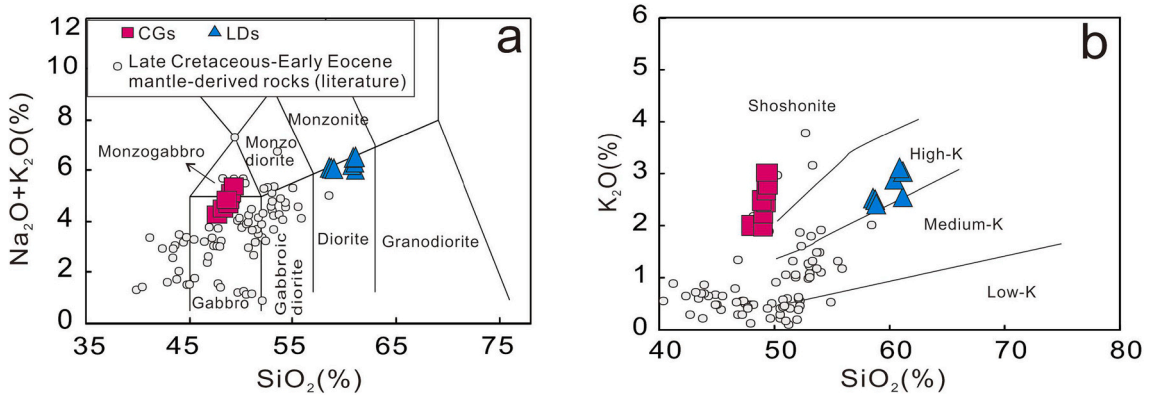

Fig. 4. (a) $Na_2O + K_2O$ (wt%) versus SiO_2 (wt%), and (b) K_2O (wt%) versus SiO_2 (wt%) plots for the CGs and LDs. All plotted data were recalculated to 100 wt% on a volatile-free basis. Data sources for Late Cretaceous–Early Eocene (100–45 Ma) mantle-derived rocks in the southern Tibet are from Mo et al. (2008); Lee et al. (2012); Ma et al. (2013a, 2013b), Qi et al. (2018), Huang et al. (2019, 2020); Wang et al. (2019).

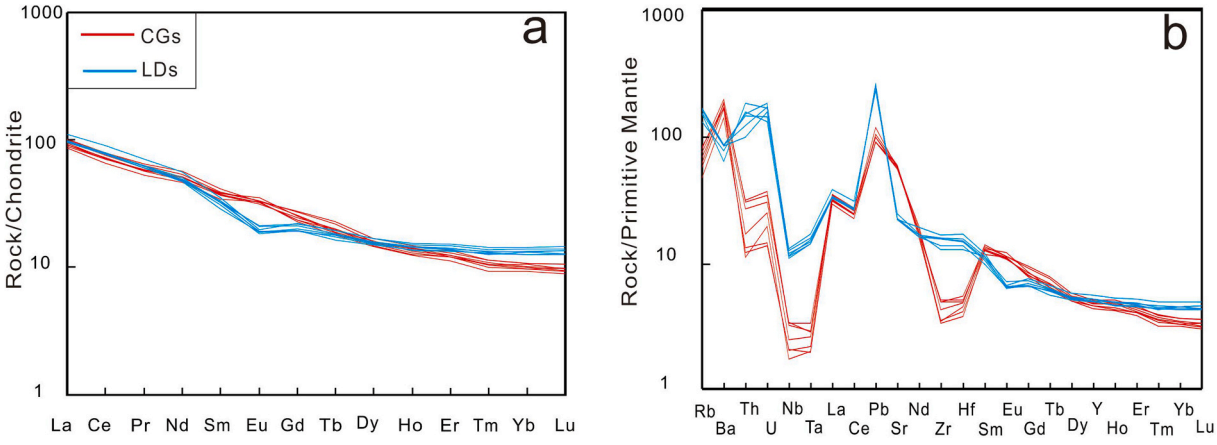

Fig. 5. (a) Chondrite-normalized REE patterns, and (b) primitive-mantle-normalized incompatible-element diagrams for the CGs and LDs. The trace-element compositions of chondrite and the primitive-mantle values are from Sun and McDonough (1989). The data sources are the same as Fig. 4.

are basaltic in composition, with low SiO_2 (48.1–49.6 wt%) and relatively high MgO (4.89–5.48 wt%) contents. They have arc-like trace element patterns with enrichment in LREEs and LILEs, and depletion in HFSEs (Fig. 5). Thus, the CGs are geochemically analogous to modern island arc basalts. There is a consensus that mafic arc magmas are generated by melting of the depleted upper mantle enriched by materials (i.e., fluids or melts) released from the subducted slab (e.g., Elliott, 2003). The CGs have depleted Nd-Hf isotopic compositions, indicating they were produced by melting of the depleted mantle. Previous studies have proposed that the HFSEs (e.g., Nb, Ta, Zr, and Hf) and HREEs (e.g.,

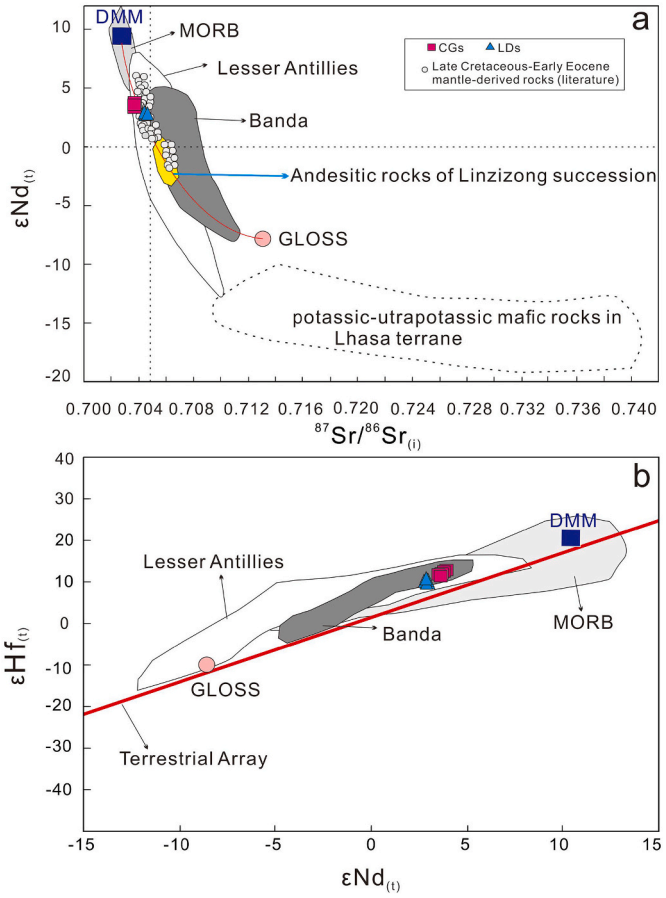

Fig. 6. Plots of (a) $\varepsilon Nd_{(t)}$ versus $^{87}Sr/^{86}Sr_{(i)}$, (b) $\varepsilon Hf_{(t)}$ versus $\varepsilon Nd_{(t)}$ for the CGs and LDs. Data source: the fields of MORB, Less Antilles and Banda arcs are from http://georoc.mpch-mainz.gwdg.de/georoc/; the field of DMM (Depleted MORB Mantle) is from Workman and Hart (2005); the field of andesitic rocks of Linzizong succession is from Mo et al. (2008), and Yan et al. (2019); and the field of post-collisional K-rich mafic rocks in the southern Tibet is from Turner et al. (1996); Miller et al. (1999); Ding et al. (2003); Gao et al. (2007); Guo et al. (2013); Liu et al. (2015). Other data sources are the same as Fig. 4.

Y and Yb) are unlikely to be transferred from the subducted slab to the mantle wedge by slab-derived fluids or melts (e.g., Elburg et al., 2002; Plank and Langmuir, 1998). This is because these elements are insoluble in fluids and depleted in slab-derived melts due to the stability of rutile, other residual Ti-bearing phases (e.g., titanite), and garnet. Therefore, HFSEs and HREEs ratios (e.g., Nb/Yb, Zr/Hf, and Nb/Ta) of mafic arc magmas are likely comparable to those of the mantle wedge before modification by the slab-derived fluids and melts. The Nb/Yb (0.8–1.4) and Y/Yb (12−13) ratios of the CGs are similar to those of MORBs (Nb/Yb = 1.0–1.5; Y/Yb ~ 11; Sun and McDonough, 1989; Pfander et al., 2007; Gale et al., 2013). Meanwhile, Zr/Hf and Nb/Ta ratios of the CGs are also similar to those of MORBs (Fig. 9a). These features indicate that the mantle source of the CGs prior to modification by the oceanic slab (oceanic crust and oceanic sediments) was likely the depleted MORB mantle (DMM). Therefore, we assume that the elemental and Sr–Nd–Hf isotopic compositions of the pre-subduction mantle beneath southern Tibet were similar to DMM.

The mantle source of mafic arc magmas is typically enriched by fluids and/or melts released from the oceanic slab, including both the oceanic crust and overlying sediments (Carpentier et al., 2009; Labanieh et al., 2010). Given that the oceanic crust is produced by melting of the depleted mantle, the fluids and/or melts released from the subducted oceanic crust usually have similar Sr–Nd–Hf isotopic compositions as MORBs (Chauvel et al., 2009; Hauff et al., 2003). In contrast, oceanic sediment-derived fluids and melts tend to have enriched Sr–Nd–Hf isotopic compositions (Chauvel et al., 2009; Plank, 2014; Vervoort et al., 1999, 2011). The CGs have Sr–Nd–Hf isotopic compositions that are more enriched than those of typical MORBs (Fig. 6), indicating their source contained contributions from subducted sediments rather than subducted oceanic crust (Chauvel et al., 2009; Elliott et al., 1997). This is because subducted sediments are the major host for incompatible elements, and adding even a small amount of sediments will dramatically change the elemental and isotopic compositions of the mantle source (Plank, 2014). This is also consistent with the fact that the CGs plot between DMM and subducted sediments on whole-rock Sr–Nd–Hf isotope diagrams (Fig. 6), and exhibit isotopic variations similar to mafic rocks from the Lesser Antilles and Banda arcs, where the mantle wedges were strongly metasomatized by subducted sediments (e.g., Labanieh et al., 2010; Nebel et al., 2011). The CGs plot within the field for global oceanic sediments on a Th/La versus Th diagram (Fig. 9b), which is also consistent with the involvement of subducted sediments in their mantle source. In addition, a subducted sediment component can account for the positive $\Delta\varepsilon Hf_{(t)}$ values of these rocks. Given that zircon-free oceanic sediment-derived melts generally have more radiogenic Hf at a given Nd isotopic composition as compared with the mantle array due to the "zircon effect" (e.g., Carpentier et al., 2009; Vervoort et al., 2011), mantle metasomatized by such sediment-derived melts will acquire the high $\Delta\varepsilon Hf_{(t)}$ values of the sediments. In the case of sediment-derived, fluid-mediated enrichment, Nd is more fluid-mobile than Hf (Hanyu et al., 2006), and the fluids can also decouple the Hf-Nd isotopic systems (Hanyu and Tatsumi, 2002; Pearce et al., 1999). Therefore, fluid-modified mantle material is likely to have less radiogenic Nd at a given Hf isotopic composition, and will also have positive $\Delta\varepsilon Hf_{(t)}$ values. Thus, the sub-arc mantle metasomatized by either subducted sediment-derived melts or fluids could generate mafic rocks with positive $\Delta\varepsilon Hf_{(t)}$ values, as is the case for the CGs. In summary, the mantle source of the CGs was a mixture source of DMM and recycled sediments.

5.2.2. *Mantle source of the LDs*

Compared with the CGs, the LDs are intermediate rocks with high SiO_2 (58.6–61.1 wt%) and low MgO (2.71–3.24 wt%) contents, and higher Mg# values (49.4–50.8) than melts directly produced by melting of the mafic crust (i.e., metabasalts; Mg# < 40; Rapp and Watson, 1995). In general, intermediate rocks with high Mg# values and depleted Sr–Nd–Hf isotopic compositions can form either by the interaction between oceanic crust-derived melts and the mantle or by FC of mantle-derived mafic melts (e.g., Defant and Drummond, 1990; Grove and Christy, 2012; Kelemen et al., 2003). Based on two main observations, we propose that the LDs did not form by the first mechanism: (1) intermediate rocks produced in this way tend to have adakitic affinities, such as high Sr/Y ratios (>20), and low Y (<18 ppm) and Yb (<1.8 ppm) contents (Defant and Drummond, 1990; Kelemen et al., 2003), in contrast to the LDs that have low Sr/Y ratios (18–22), and high Y (22.9–25.7 ppm) and Yb (2.1–2.5 ppm) contents; (2) compared with andesitic rocks of the Linzizong volcanic succession, which were produced by partial melting of Neo-Tethyan oceanic crust (Mo et al., 2008), the LDs have markedly more depleted Sr-Nd isotopic compositions (Fig. 6a). As such, the LDs most likely formed by FC of mantle-derived mafic melts. Based on the following observations, we propose that the LDs were generated by melting of a mantle source that was similar to the CGs: (1) the LDs were produced in the Gangdese continental arc setting, and exhibit arc-like trace element patterns (Fig. 5b) and Sr–Nd–Hf isotopic compositions similar to those of the CGs; (2) Zr/Hf and Nb/Ta ratios of the LDs are comparable to those of MORBs (Fig. 9a), indicating their mantle prior to modification by oceanic slab (oceanic crust and oceanic sediments)-derived fluids and melts was similar to DMM, and the high Th contents and Th/La values of the LDs require a sediment component in their mantle source (Fig. 9b). Therefore, we propose that the mantle source of the LDs was also a mixture source of DMM and recycled oceanic sediments.

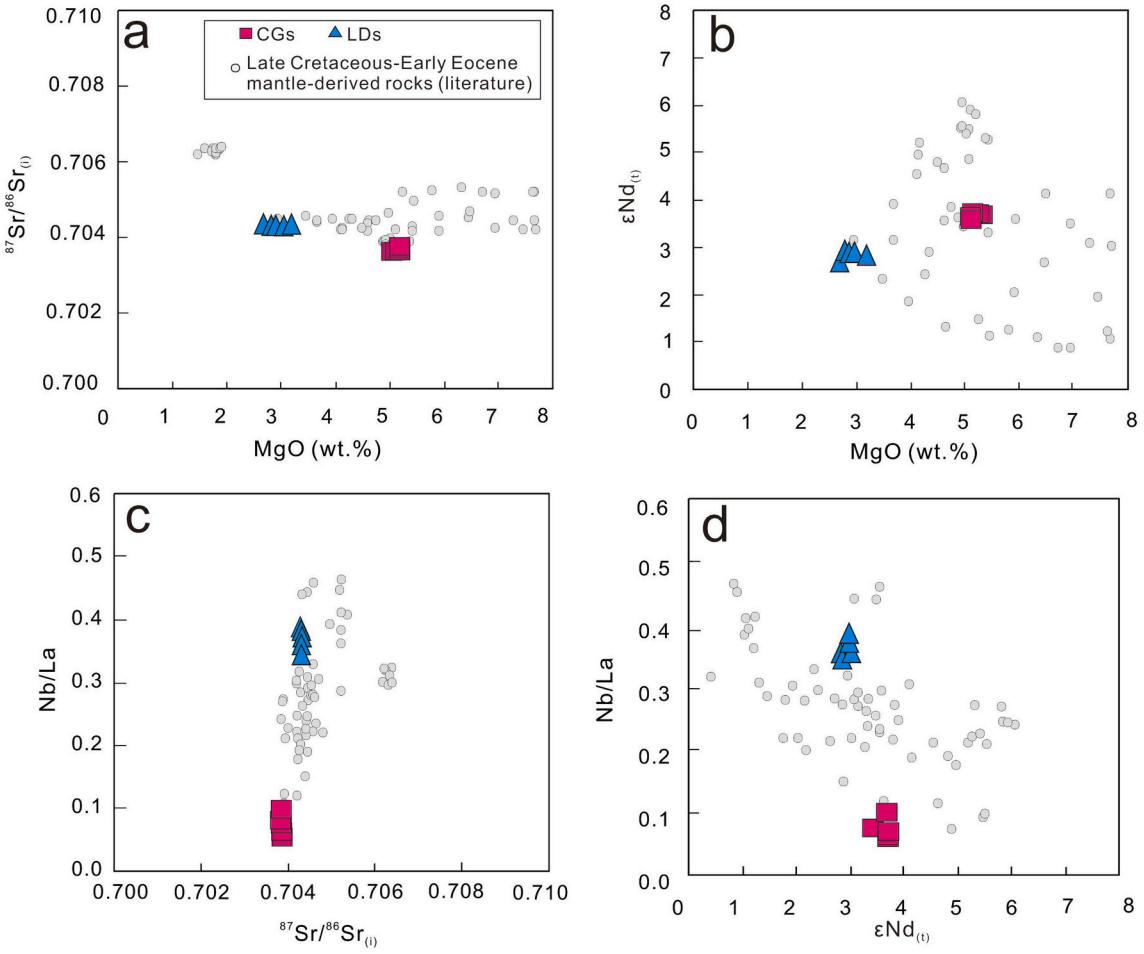

Fig. 7. Plots of (a) $^{87}Sr/^{86}Sr_{(i)}$, versus MgO (wt%), (b) $\varepsilon Nd_{(t)}$ versus MgO (wt%), and (c) Nb/La versus $^{87}Sr/^{86}Sr_{(i)}$, and (d) Nb/La versus $\varepsilon Nd_{(t)}$ for the CGs and LDs. The data sources are the same as Fig. 4.

5.3. *Mantle enrichment by sediment-derived fluids or melts*

In general, oceanic sediment-derived fluids are enriched in LILEs and Pb, whereas oceanic sediment-derived melts are characterized by significant enrichment in Th and LREEs (Elliott et al., 1997; Johnson and Plank, 1999; Pearce et al., 1999). The high Ba, U, Pb, and Sr, and low Th contents of the CGs (Fig. 5b), suggest their mantle source contains subducted oceanic sediment-derived fluids rather than melts (Johnson and Plank, 1999; Pearce and Stern, 2006). This is consistent with their high Sr/Th, Ba/La, and Ba/Th, but low Th/Nd, Th/Yb, Th/Sm, and Th/Ce ratios (Fig. 10; Woodhead et al., 1998; Hanyu et al., 2006). In contrast, the LDs are enriched in Th (Fig. 5b), denoting the involvement of subducted oceanic sediment-derived melts in their mantle source, because Th is immobile in fluids (Hermann and Spandler, 2008). The LDs have high Th/Nd, Th/Yb, Th/Sm, and Th/Ce ratios, and low Sr/Th, Ba/La, and Ba/Th ratios (Fig. 10), indicating that their mantle source was enriched by the subducted sediment-derived melts. Thus, the CGs likely represent partial melts of DMM that had been enriched by fluids from subducted sediments, whereas the LDs were produced by melting of DMM that had been enriched by melts from subducted sediments. To further estimate the proportion of subducted sediment-derived components in the mantle source of the CGs and LDs, we carried out modeling of Ba/La and Nd-Hf isotope ratios using an approach similar to Guo et al. (2016). The results indicate that the CGs could have been generated by melting of DMM enriched by 3%–4% sediment-derived fluids and the LDs could result from melting of DMM enriched by 1.5%–2.5% sediment-derived melts (Fig. 11).

Given that the CGs and LDs were sampled in the central–southern Lhasa Terrane (87–92.5°E) (Fig. 1), and in order to better constrain how the subducted slab-derived components geochemically modified the local mantle beneath southern Tibet during the late stage (100–45 Ma) of Neo-Tethyan slab subduction, we compiled previously published data for mantle-derived mafic–intermediate rocks during this time in the central–southern Lhasa Terrane (Huang et al., 2019, 2020; Lee et al., 2012; Ma et al., 2013a, 2013b; Mo et al., 2008; Qi et al., 2018; Wang et al., 2019). The Sr-Nd isotope data for these mafic–intermediate rocks plot along a mixing line between DMM and subducted sediments, and have a large range of Sr-Nd isotope ratios similar to mafic igneous rocks from the Lesser Antilles and Banda arcs (Fig. 6). This indicates that subducted oceanic sediments were present in their mantle source. Meanwhile, the Sr/Th, Ba/La, Ba/Th, Th/Ce, and Th/Sm ratios of these mafic–intermediate rocks plot between those of the CGs and LDs (Fig. 10), also suggesting the involvement of subducted sediments in their source was in the form of fluids and/or melts. Therefore, intensive dehydration and melting of subducted oceanic sediments occurred in the late stage (100–45 Ma) of Neo-Tethyan slab subduction beneath the study area.

5.4. *Thermal events responsible for generating the CGs and LDs*

The Lhasa Terrane records the subduction of the Neo-Tethyan oceanic lithosphere, subsequent collision of the Indian and Asian continents, and subduction of Indian continental lithosphere (e.g., Chung et al., 2005). These events were accompanied by a series of geodynamic

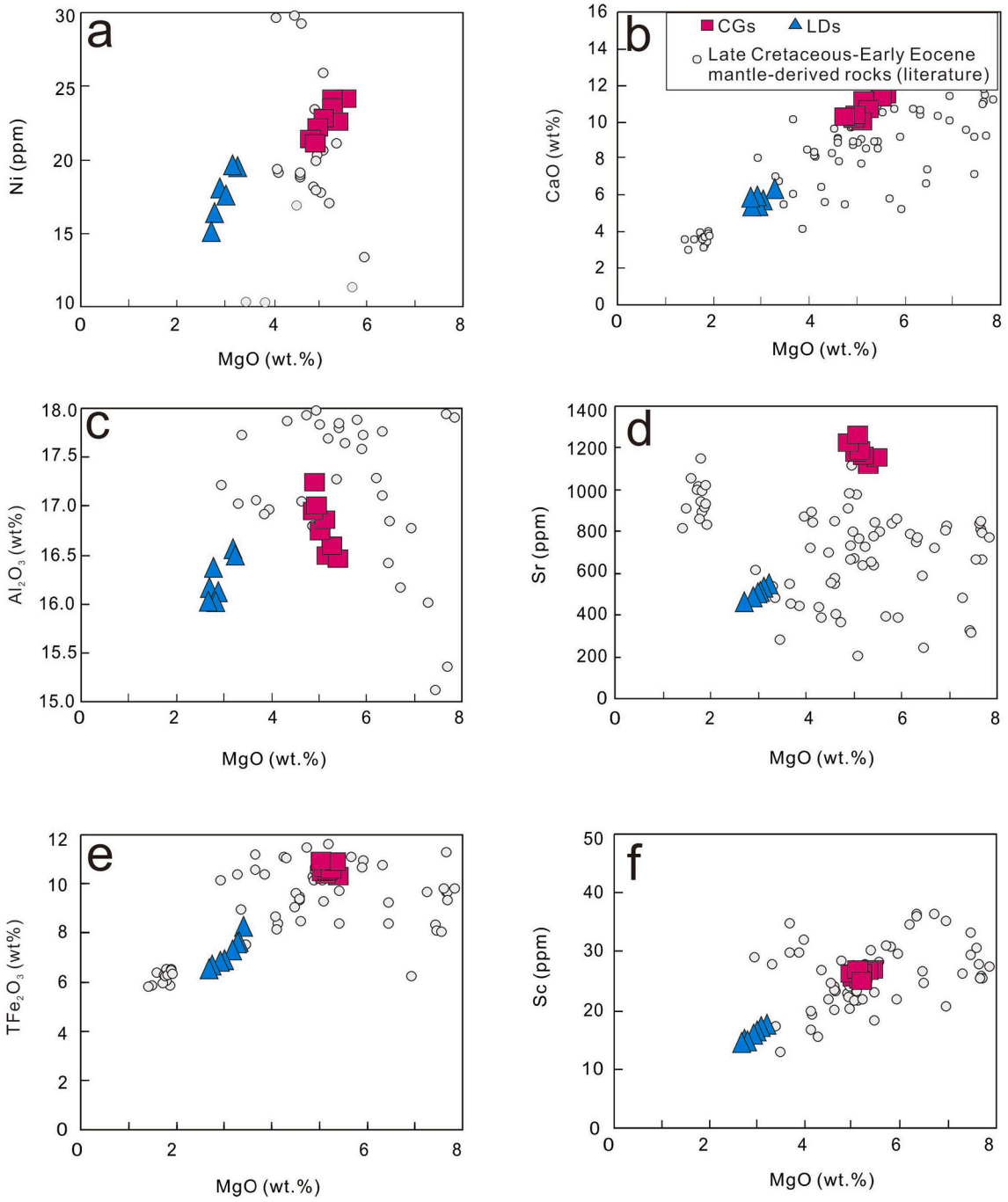

Fig. 8. Variations in (a) Ni (ppm) versus MgO (wt%), (b) CaO (wt%) versus MgO (wt%), (c) Al_2O_3 (wt%) versus MgO (wt%), (d) Sr (ppm) versus MgO (wt%), (e) TFe_2O_3 (wt%) versus MgO (wt%), and (f) Sc (ppm) versus MgO (wt%) for the CGs and LDs, respectively. The data sources are the same as Fig. 4.

processes, including oceanic ridge subduction, slab rollback, and break-off of the subducted oceanic plate (e.g., Chung et al., 2005; Zhu et al., 2013). Based on the occurrence of high-temperature charnockites and granulite-facies metamorphism of the surrounding metamorphic rocks at 90 ± 5 Ma, it has been suggested that Neo-Tethyan oceanic ridge subduction may have occurred during 100–90 Ma (e.g., Zhang et al., 2010). The abrupt decrease in the convergence rate between India and Asia, exhumation of ultra-high-pressure rocks, exposure of ocean island basalt (OIB)-like mafic rocks, and rapid addition of juvenile material in the Lhasa Terrane during 53–45 Ma suggest that that slab break-off of the subducted Neo-Tethyan slab may have taken place during this period (e.g., Ji et al., 2016; Leech et al., 2005; Zhu et al., 2013, 2015). Both ridge subduction and slab break-off can rapidly alter the thermal state of a subducted slab due to the upwelling of hot asthenosphere (Davies and von Blanckenburg, 1995; Thorkelson and Breitsprecher, 2005). The ascending hot asthenosphere can heat an overlying subduction zone and result in extensive melting and dehydration of oceanic sediments. Therefore, dehydration and melting of subducted oceanic sediments beneath the study area may have been ubiquitous in the late stage (100–45 Ma) of Neo-Tethyan oceanic slab subduction, which is a common phenomenon in subduction systems with a high geothermal gradient (e.g., Watt et al., 2013).

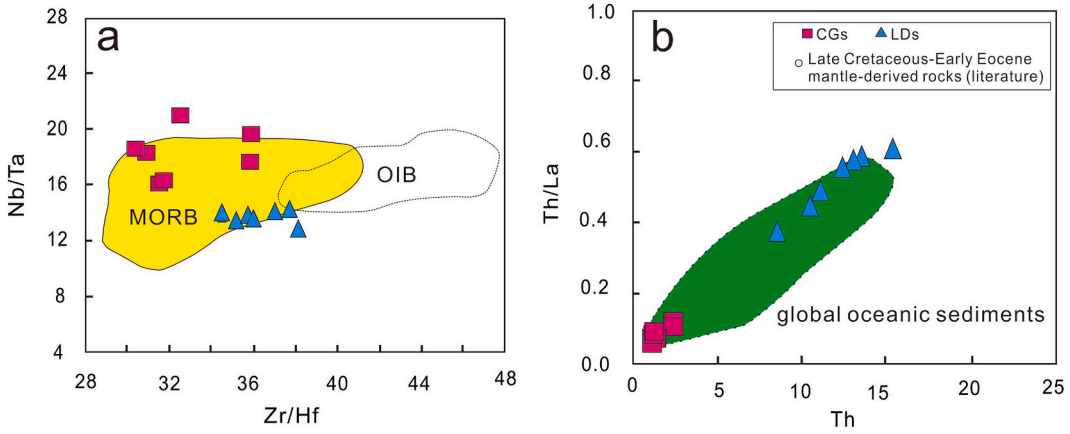

Fig. 9. Diagrams of (a) Nb/Ta versus Zr/Hf, and (b) Th/La versus Th (ppm) for the CGs and LDs. Data sources are as follows: the field of MORB are from Sun and McDonough (1989), Workman and Hart (2005); and Pfander et al. (2007); the field of OIB is from Sun and McDonough (1989); Pfander et al. (2007); and Gale et al. (2013) the field of global sediments is from Plank (2014).

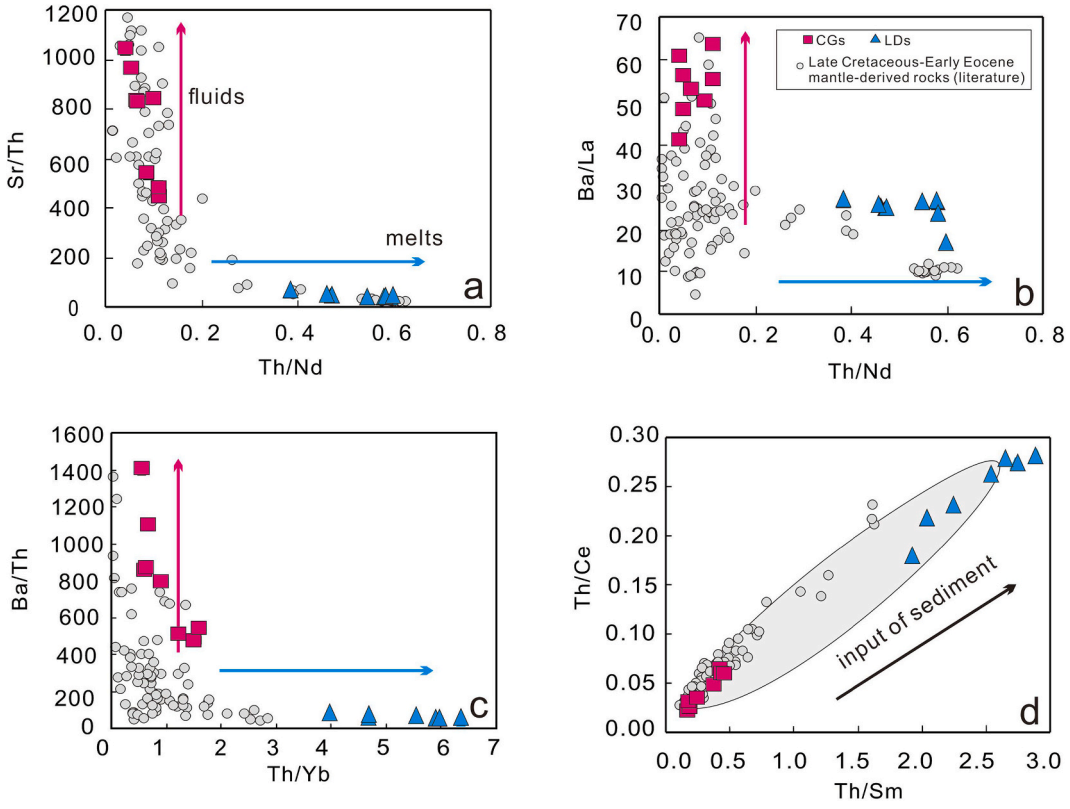

Fig. 10. Plots of (a) Sr/Th versus Th/Nd, (b) Ba/La versus Th/Nd, (c) Ba/Th versus Th/Yb, and (d) Th/Ce versus Th/Sm for the CGs and LDs. The data sources are the same as Fig. 4.

5.5. Implications for the Miocene isotopically enriched mantle beneath the Lhasa Terrane

The Miocene post-collisional K-rich mafic rocks are widely distributed in the western Lhasa Terrane (west of 87°E) and have highly enriched Sr-Nd isotopic compositions, indicating they formed by melting of an isotopically enriched mantle source. This isotopically enriched mantle source is argued to have been generated by the subduction of either the Neo-Tethyan oceanic slab or Indian continental slab (e.g., Ding et al., 2003; Gao et al., 2007; Tommasini et al., 2010; Guo et al., 2013; Liu et al., 2015).

As we discussed in Section 5.2, the addition of sediments can dramatically change the elemental and isotopic compositions of mantle source. Our study has shown that melting and/or dehydration of oceanic sediments occurred mainly during the late stage (100–45 Ma) of Neo-Tethyan oceanic slab subduction. This means that the mantle beneath the Lhasa Terrane was most likely enriched during 100–45 Ma. The CGs and LDs, and previously studied mafic–intermediate igneous rocks during this time in the central–southern (87–92.5°E) Lhasa Terrane, have depleted Sr-Nd isotopic compositions, which are distinct from the Miocene post-collisional K-rich mafic rocks that have enriched Sr-Nd isotopic compositions (Fig. 6). This indicates that the mantle beneath the Lhasa Terrane (at least the central–southern Lhasa Terrane) was still depleted, even though the mantle source had been enriched during

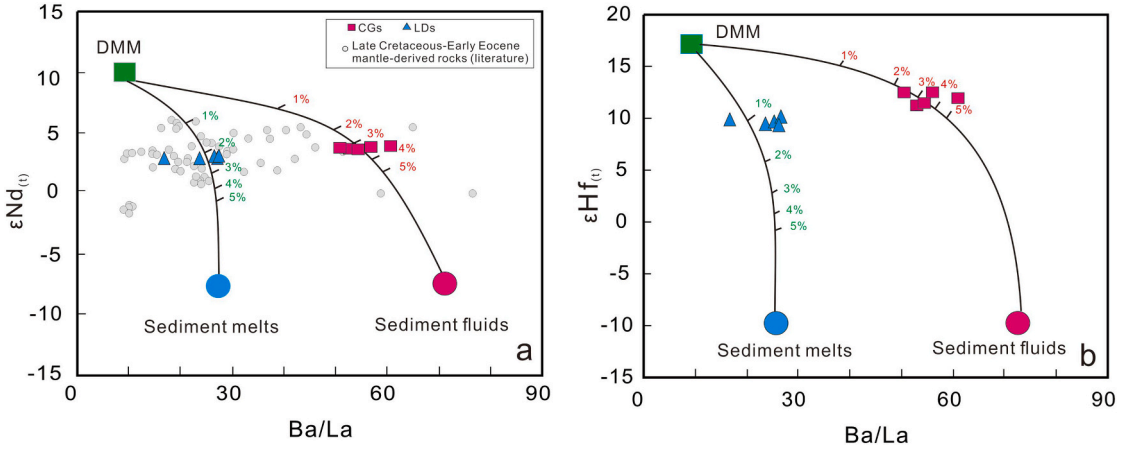

Fig. 11. Diagrams of (a) $\varepsilon Nd_{(t)}$ versus Ba/La, and (b) $\varepsilon Hf_{(t)}$ versus Ba/La for CGs and LDs. Date source: the data of DMM (Ba = 3, La = 0.4, $\varepsilon Nd_{(t)} = +18$, and $\varepsilon Hf_{(t)} = +10$) are from Workman and Hart (2005). The data of the subducted sediment (Ba = 720, La = 26, $\varepsilon Nd_{(t)} = -8$, and $\varepsilon Hf_{(t)} = -10$) are from Plank (2014). The bulk partition coefficients (KD) during sediment melting, the elemental mobility in aqueous fluid and the dehydration volume released from sediment are followed from Guo et al. (2016). Other data sources are the same as Fig. 4.

subduction of the Neo-Tethyan oceanic slab. This demonstrates that simply melting of the mantle source that had been enriched by oceanic sediments beneath the Lhasa Terrane could not have produced the K-rich mafic rocks. To account for the enriched component of K-rich mafic rocks in the Lhasa Terrane, we invoke that there may be at least two possibilities: (1) prior to Neo-Tethyan oceanic slab subduction, the mantle beneath the central–southern and western Lhasa Terrane had distinct geochemical characteristics. For example, prior to Neo-Tethyan oceanic slab subduction, the mantle beneath the western Lhasa Terrane may have been an ancient Proterozoic isotopically enriched mantle as proposed in previous studies (e.g., Miller et al., 1999; Turner et al., 1996), in contrast to the DMM beneath the central-southern Lhasa Terrane as inferred in this study. This ancient isotopically enriched mantle beneath the western Lhasa Terrane was the enriched source of the K-rich mafic rocks; (2) given that underthrusting of Indian continental lithosphere followed the India–Asia collision (Freymueller, 2011), it is apparent that Indian continent crust may have metasomatized the source region of the K-rich mafic rocks (Ding et al., 2003). However, it is beyond the scope of this study to demonstrate whether ancient mantle or Indian continent crust was the enriched component in the source of the K-rich mafic rocks. Our study clearly stresses that the enriched component of these K-rich mafic rocks cannot be simply attributed to materials derived from the Neo-Tethyan oceanic slab, and other components are required to account for the enriched source of these K-rich mafic rocks.

6. Conclusions

Based on new geochronological, geochemical, and Sr–Nd–Hf isotope data for two plutons (CGs and LDs), along with previously published data, we examined how the mantle was geochemically modified during the late stage (100–45 Ma) of Neo-Tethyan oceanic slab subduction beneath the Lhasa Terrane. The geochemical characteristics of the CGs and LDs indicate that they were produced by melting of DMM that had been enriched by oceanic sediment-derived fluids and melts, respectively. Our and previous studies suggest that dehydration and melting of subducted Neo-Tethyan oceanic sediments may have commonly occurred in the late stage (100–45 Ma) of Neo-Tethyan oceanic slab subduction beneath the study area. This is a common phenomenon in relatively hot subduction zones, such as the Lesser Antilles and Banda arcs. Although oceanic sediments would have dramatically changed the elemental and isotopic compositions of the mantle source, the mantle beneath the Lhasa Terrane was still isotopically relatively depleted as compared with the mantle source of post-collisional K-rich mafic rocks in the Lhasa Terrane. This demonstrates that the enriched component in the mantle source of the K-rich mafic rocks cannot be simply attributed to Neo-Tethyan oceanic slab subduction, and requires additional materials in their mantle source.

Declaration of Competing Interest

The authors declare that they have no competing financial interests or personal relationships that could have appeared to influence the work in this paper.

Acknowledgments

We would like to thank the editor and reviewers for their constructive and thoughtful comments. This research was financially supported by the Ministry of Science and Technology of the People's Republic of China (020YFA0714804, 2019QZKK0703) and Natural Science Foundation of China (41873037, 92055206). This is contribution No. IS-3092 from GIGCAS.

Appendix A. Supplementary data

Supplementary data to this article can be found online at https://doi.org/10.1016/j.lithos.2021.106505.

References

Andersen, T., 2002. Correction of common lead in U–Pb analyses that do not report ^{204}Pb. Chem. Geol. 192, 59–79.
Carpentier, M., Chauvel, C., Maury, R.C., Mattielli, N., 2009. The "zircon effect" as recorded by the chemical and Hf isotopic compositions of Lesser Antilles forearc sediments. Earth Planet. Sci. Lett. 287, 86–99.
Castro, A., Vogt, K., Gerya, T.V., 2013. Generation of new continental crust by sublithospheric silicic-magma relamination in arcs: a test of Taylor's andesite model. Gondwana Res. 23, 1554–1566.
Chauvel, C., Marini, J.C., Plank, T., Ludden, J.N., 2009. Hf-Nd input flux in the Izu-Mariana subduction zone and recycling of subducted material in the mantle. Geochem. Geophys. Geosyst. 10, Q01001 https://doi.org/10.1029/2008GC002101.
Chung, S.L., Chu, M.F., Zhang, Y., Xie, Y., Lo, C.H., Lee, T.Y., Lan, C.Y., Li, X., Zhang, Q., Wang, Y., 2005. Tibetan tectonic evolution inferred from spatial and temporal variations in post-collisional magmatism. Earth Sci. Rev. 68, 173–196.
Davies, J.H., von Blanckenburg, F., 1995. Slab breakoff: a model of lithosphere detachment and its test in the magmatism and deformation of collisional orogens. Earth Planet. Sci. Lett. 129, 85–102.
Defant, M.J., Drummond, M.S., 1990. Derivation of some modern arc magmas by melting of young subducted lithosphere. Nature. 347, 662–665.
Dewey, J.F., Shackleton, R.M., Chengfa, C., Yiyin, S., 1988. The tectonic evolution of the Tibetan Plateau. Philos. Trans. R. Soc. Lond. Ser. A Math. Phys. Sci. 327, 379–413.

Ding, L., Kapp, P., Zhong, D.L., Deng, W.M., 2003. Cenozoic volcanism in Tibet: evidence for a transition from oceanic to continental subduction. J. Petrol. 44, 1833–1865.
Elburg, M.A., Bergen, M.A., Hoogewerff, J., Foden, J., Vroon, P., Zulkarnain, I., Nasution, A., 2002. Geochemical trends across an arc-continent collision zone: magma sources and slab-wedge transfer processes below the Pantar Strait volcanoes, Indonesia. Geochim. Cosmochim. Acta 66, 2771–2789.
Elliott, T., 2003. Tracers of the slab. In: Eiler, J. (Ed.), Inside the Subduction Factory. Geophysical Monograph, 138. American Geophysical Union, Washington DC, pp. 23–45.
Elliott, T., Plank, T., Zindler, A., White, W., Bourdon, B., 1997. Element transport from slab to volcanic front at the Mariana arc. J. Geophys. Res. Solid Earth 102, 14991–15019.
Ernst, W.G., 2005. Alpine and Pacific styles of Phanerozoic mountain building: subduction-zone petrogenesis of continental crust. Terra Nova 17, 165–188.
Freymueller, J.T., 2011. Earth science. A new mechanical model for Tibet. Nature 472, 48–49.
Gale, A., Dalton, C.A., Langmuir, C.H., Su, Y., Schilling, J.G., 2013. The mean composition of ocean ridge basalts. Geochem. Geophys. Geosyst. 14 (3), 489–518.
Gao, Y.F., Hou, Z.Q., Kamber, B.S., Wei, R.H., Meng, X.J., Zhao, R.S., 2007. Lamproitic rocks from a continental collision zone: evidence for recycling of subducted Tethyan oceanic sediments in the mantle beneath southern Tibet. J. Petrol. 48, 729–752.
Grove, T.L., Christy, B.T., 2012. The role of H_2O in subduction zone magmatism. Annu. Rev. Earth Planet. Sci. 40, 413–439.
Guo, Z.F., Wilson, M., Zhang, M.L., Cheng, Z.H., Zhang, L.H., 2013. Post-collisional, K-rich mafic magmatism in south Tibet: constraints on Indian slab-to-wedge transport processes and plateau uplift. Contrib. Mineral. Petrol. 165, 1311–1340.
Guo, F., Li, H.X., Fan, W.M., Li, J.Y., Zhao, L., Huang, M.W., 2016. Variable sediment flux in generation of Permian subduction-related mafic intrusions from the Yanbian region, NE China. Lithos 261, 195–215.
Hanyu, T., Tatsumi, Y., 2002. A contribution of slab-melts to the formation of high-Mg andesite magmas; Hf isotopic evidence from SW Japan. Geophys. Res. Lett. 29, 2051.
Hanyu, T., Tatsumi, Y., Nakai, S.I., Chang, Q., Miyazaki, T., Sato, K., Tani, K., Shibata, T., Yoshida, T., 2006. Contribution of slab melting and slab dehydration to magmatism in the NE Japan arc for the last 25 Myr: Constraints from geochemistry. Geochem. Geophys. Geosyst. 7, Q08002. https://doi.org/10.1029/2005GC001220.
Hauff, F., Hoernle, K., Schmidt, A., 2003. Sr-Nd-Pb composition of Mesozoic Pacific oceanic crust (Site 1149 and 801, ODP Leg 185), Implications for alteration of ocean crust and the input into the Izu-Bonin-Mariana subduction system. Geochem. Geophys. Geosyst. 4 (8), 8913.
Hermann, J., Spandler, C.J., 2008. Sediment melts at sub-arc depths: an experimental study. J. Petrol. 49, 717–740.
Hu, X., Garzanti, E., Wang, J., Huang, W., An, W., Webb, A., 2016. The timing of India-Asia collision onset - facts, theories, controversies. Earth Sci. Rev. 160, 264–299.
Huang, F., Zhang, Z., Xu, J., Li, X., Zeng, Y., Wang, B., Li, X., Xu, R., Fan, Z., Tian, Y., 2019. Fluid flux in the lithosphere beneath southern Tibet during NeoTethyan slab breakoff: evidence from an appinite– granite suite. Lithos 344–345, 324–338.
Huang, F., Rooney, T., Xu, J.F., Zeng, Y.C., 2020. Magmatic record of continuous Neo-Tethyan subduction after initial India-Asia collision in the central part of southern Tibet. GSA Bull. https://doi.org/10.1130/B35444.1.
Ji, W.Q., Wu, F.Y., Chung, S.L., Li, J.X., Liu, C.Z., 2009. Zircon U-Pb geochronology and Hf isotopic constraints on petrogenesis of the Gangdese batholith, southern Tibet. Chem. Geol. 262, 229–245.
Ji, W.Q., Wu, F.Y., Chung, S.L., Wang, X.C., Liu, C.Z., Li, Q.L., Liu, Z.C., Liu, X.C., Wang, J.G., 2016. Eocene Neo-Tethyan slab breakoff constrained by 45 Ma oceanic island basalt–type magmatism in southern Tibet. Geology 44, 283–286.
Johnson, M.C., Plank, T., 1999. Dehydration and melting experiments constrain the fate of subducted sediments. Geochem. Geophys. Geosyst. 1, 1007. https://doi.org/10.1029/1999GC000014.
Kang, Z.Q., Xu, J.F., Wilde, S.A., Feng, Z.H., Chen, J.L., Wang, B.D., Fu, W.C., Pan, H.B., 2014. Geochronology and geochemistry of the Sangri Group Volcanic Rocks, Southern Lhasa Terrane: implications for the early subduction history of the Neo-Tethys and Gangdese Magmatic Arc. Lithos 200 (201), 157–168.
Kelemen, P.B., Hanghoj, K., Greene, A.R., 2003. One view of the geochemistry of subduction-related magmatic arcs, with an emphasis on primitive andesites and lower crust. Treat. Geochem. 3, 593–659.
Labanieh, S., Chauvel, C., Germa, A., Quidelleur, X., Lewin, E., 2010. Isotopic hyperbolas constrain sources and processes under the Lesser Antilles arc. Earth Planet. Sci. Lett. 298, 35–46.
Lee, H.Y., Chung, S.L., Ji, J.Q., Qian, Q., Galleta, S., Lo, C.H., Lee, T.Y., Zhang, Q., 2012. Geochemical and Sr–Nd isotopic constraints on the genesis of the Cenozoic Linzizong volcanic successions, southern Tibet. J. Asian Earth Sci. 53, 96–114.
Leech, M.L., Singh, S., Jain, A., Klemperer, S.L., Manickavasagam, R., 2005. The onset of India-Asia continental collision: early, steep subduction required by the timing of UHP metamorphism in the western Himalaya. Earth Planet. Sci. Lett. 234, 83–97.
Liu, D., Zhao, Z.D., Zhu, D.C., Niu, Y.L., Widom, E., Teng, F.Z., DePaolo, D.J., Ke, S., Xu, J.F., Wang, Q., Mo, X.X., 2015. Identifying mantle carbonatite metasomatism through Os–Sr–Mg isotopes in Tibetan ultrapotassic rocks. Earth Planet. Sci. Lett. 430, 458–469.
Ludwig, K.R., 2003. User's Manual for Isoplot 3.00. A Geochronological Toolkit for Microsoft Excel. Berkeley Geochronology Center, Berkeley, CA. Special Publication No. 4a.
Ma, L., Wang, Q., Li, Z.X., Wyman, D.A., Jiang, Z.Q., Yang, J.H., Gou, G.N., Guo, H.F., 2013a. Early Late Cretaceous (ca. 93 Ma) norites and hornblendites in the Milin area, eastern Gangdese: Lithosphere–asthenosphere interaction during slab roll-back and an insight into early Late Cretaceous (ca. 100–80 Ma) magmatic "flare-up" in southern Lhasa (Tibet). Lithos. 172-173, 17–30.
Ma, L., Wang, Q., Li, Z.X., Wyman, D.A., Jiang, Z.Q., Yang, J.H., Li, Q.L., Gou, G.N., Guo, H.F., 2013b. Late Cretaceous crustal growth in the Gangdese area, southern Tibet: petrological and Sr-Nd-Hf-O isotopic evidence from Zhengga diorite-gabbro. Chem. Geol. 349-350, 54–70.
Meng, Y., Xu, Z., Santosh, M., Ma, X., Chen, X., Guo, G., Liu, F., 2015. Late Triassic crustal growth in southern Tibet: evidence from the Gangdese magmatic belt. Gondwana Res. 37, 449–464.
Miller, C., Schuster, R., Klotzli, U., Frank, W., Purtscheller, F., 1999. Post-collisional potassic and ultrapotassic magmatism in SW Tibet: geochemical and Sr-Nd-Pb-O isotopic constraints for mantle source characteristics and petrogenesis. J. Petrol. 40, 1399–1424.
Mo, X.X., Hou, Z.Q., Niu, Y.L., Dong, G.C., Qu, X.M., Zhao, Z.D., Yang, Z.M., 2007. Mantle contributions to crustal thickening during continental collision: evidence from Cenozoic igneous rocks in southern Tibet. Lithos 96, 225–242.
Mo, X.X., Niu, Y.L., Dong, G.C., Zhao, Z.D., Hou, Z.Q., Zhou, S., Ke, S., 2008. Contribution of syncollisional felsic magmatism to continental crust growth: a case study of the Paleogene Linzizong volcanic Succession in southern Tibet. Chem. Geol. 250, 49–67.
Nebel, O., Vroon, P.Z., van Westrenen, W., Iizuka, T., Davies, G.R., 2011. The effect of sediment recycling in subduction zones on the Hf isotope character of new arc crust, Banda arc, Indonesia. Earth Planet. Sci. Lett. 303, 240–250.
Pearce, J.A., Stern, R.J., 2006. Origin of back-arc basin magmas: trace element and isotope perspectives. Geophys. Monogr. Am. Geophys. Union 166, 63–86.
Pearce, J.A., Kempton, P.D., Nowell, G.M., Noble, S.R., 1999. Hf–Nd element and isotope perspective on the nature and provenance of mantle and subduction components in western Pacific arc-basin systems. J. Petrol. 40, 1579–1611.
Pfander, J.A., Munker, C., Stracke, A., Mezger, K., 2007. Nb/Ta and Zr/Hf in ocean island basalts-implications for crust-mantle differentiation and the fate of Niobium. Earth Planet. Sci. Lett. 254, 158–172.
Plank, T., 2014. 4.17 - The chemical composition of subducting sediments. In: Holland, H.D., Turekian, K.K. (Eds.), Treatise on Geochemistry, Second edition. Elsevier, Oxford, pp. 607–629.
Plank, T., Langmuir, C., 1998. The chemical composition of subducting sediment and its consequences for the crust and mantle. Chem. Geol. 145, 325–394.
Qi, Y., Gou, G.N., Wang, Q., Wyman, D.A., Jiang, Z.Q., Li, Q.L., Zhang, L., 2018. Cenozoic mantle composition evolution of southern Tibet indicated by Paleocene (~64 Ma) pseudoleucite phonolitic rocks in central Lhasa Terrane. Lithos 302-303, 178–188.
Rapp, R.P., Watson, E.B., 1995. Dehydration melting of metabasalt at 8-32 kbar: implications for continental growth and crust-mantle recycling. J. Petrol. 36, 891–931.
Rudnick, R.L., Gao, S., 2003. Composition of the continental crust. In: Rudnick, R.L. (Ed.), The Crust: Treaties on Geochemistry, 3. Elsevier, Amsterdam (1–64 pp.).
Singer, B.S., Jicha, B.R., Leeman, W.P., Rogers, N.W., Thirlwall, M.F., Ryan, J., Nicolaysen, K.E., 2007. Along-strike trace element and isotopic variation in Aleutian Island arc basalt: Subduction melts sediments and dehydrates serpentine. J. Geophys. Res. Solid Earth 112, B06206. https://doi.org/10.1029/2006JB004897.
Sun, S.S., McDonough, W.F., 1989. Chemical and isotopic systematics of oceanic basalts: implications for mantle composition and processes. Geol. Soc. Lond., Spec. Publ. 42, 313–345.
Thorkelson, D.J., Breitsprecher, K., 2005. Partial melting of slab window margins: genesis of adakitic and non-adakitic magmas. Lithos 79, 25–41.
Tommasini, S., Avanzinelli, R., Conticelli, S., 2010. The Th/La and Sm/La conundrum of the Tethyan realm lamproites. Earth Planet. Sci. Lett. 301, 469–478.
Turner, S., Arnaud, N., Liu, J., Rogers, N., Hawkesworth, C., Harris, N., Kelley, S., Van Calsteren, P., Deng, W., 1996. Postcollision, shoshonitic volcanism on the Tibetan Plateau: implications for convective thinning of the lithosphere and the source of ocean island basalts. J. Petrol. 37, 45–71.
Vervoort, J.D., Blichert-Toft, J., Patchett, P.J., Albarede, F., 1999. Relationships between Lu– Hf and Sm–Nd isotopic systems in the global sedimentary system. Earth Planet. Sci. Lett. 168, 79–99.
Vervoort, J.D., Plank, T., Prytulak, J., 2011. The Hf–Nd isotopic composition of marine sediments. Geochim. Cosmochim. Acta 75, 5903–5926.
Wang, Y.F., Zeng, L.S., Gao, J.H., Zhao, L.H., Gao, L.E., Shang, Z., 2019. Along-arc variations in isotope and trace element compositions of Paleogene gabbroic rocks in the Gangdese batholith, southern Tibet. Lithos 324, 877–892.
Watt, S.F.L., Pyle, D.M., Mather, T.A., Naranjo, J.A., 2013. Arc magma compositions controlled by linked thermal and chemical gradients above the subducting slab. Geophys. Res. Lett. 40, 2550–2556.
Wilson, M., 1989. Igneous petrogenesis. Unwin Hyman, London, p. 466.
Woodhead, J.D., Eggins, S.M., Johnson, R.W., 1998. Magma genesis in the New Britain island arc: further insights into melting and mass transfer processes. J. Petrol. 39, 1641–1668.
Workman, R.K., Hart, S.R., 2005. Major and trace element composition of the depleted MORB mantle (DMM). Earth Planet. Sci. Lett. 231, 53–72.
Yan, H., Long, X., Li, J., Wang, Q., Zhao, B., Shu, C., Gou, L., Zuo, R., 2019. Arc andesitic rocks derived from partial melts of mélange diapir in subduction zones: evidence from whole-rock geochemistry and Sr-Nd-Mo isotopes of the Paleogene Linzizong volcanic succession in southern Tibet. J. Geophys. Res. Solid Earth 124, 456–475.
Yin, A., Harrison, T.M., 2000. Geologic evolution of the Himalayan–Tibetan orogen. Annu. Rev. Earth Planet. Sci. 28, 211–280.
Zhang, Z.M., Zhao, G.C., Santosh, M., Wang, J.L., Dong, X., Shen, K., 2010. Late Cretaceous charnockite with adakitic affinities from the Gangdese batholith, southeastern Tibet: evidence for Neo-Tethyan mid-ocean ridge subduction? Gondwana Res. 17, 615–631.
Zheng, Y.F., Chen, Y.X., 2016. Continental versus oceanic subduction zones. Natl. Sci. Rev. 3, 495–519.

Zhu, D.C., Pan, G.T., Chung, S.L., Liao, Z.L., Wang, L.Q., Li, G.M., 2008. SHRIMP zircon age and geochemical constraints on the origin of lower Jurassic volcanic rocks from the Yeba Formation, Southern Gangdese, South Tibet. Int. Geol. Rev. 50, 442–471.
Zhu, D.C., Zhao, Z.D., Niu, Y.N., Mo, X.X., Chung, S.L., Hou, Z.Q., Wang, L.Q., Wu, F.Y., 2011. The Lhasa terrane: record of a microcontinent and its histories of drift and growth. Earth Planet. Sci. Lett. 301, 241–255.
Zhu, D.C., Zhao, Z.D., Niu, Y.N., Dilek, Y., Hou, Z.Q., Mo, X.X., 2013. Origin and pre-Cenozoic evolution of the Tibetan Plateau. Gondwana Res. 23, 1429–1454.
Zhu, D.C., Wang, Q., Zhao, Z.D., Chung, S.L., Cawood, P.A., Niu, Y.L., Liu, S.A., Wu, F.Y., Mo, X.X., 2015. Magmatic record of India-Asia collision. Sci. Rep. 5, 14289. https://doi.org/10.1038/srep14289.
Zong, K.Q., Klemd, R., Yuan, Y., He, Z.Y., Guo, J.L., Shi, X.L., Liu, Y.S., Hu, Z.C., Zhang, Z.M., 2017. The assembly of Rodinia: the correlation of early Neoproterozoic (ca. 900 Ma) high-grade metamorphism and continental arc formation in the southern Beishan Orogen, southern Central Asian Orogenic Belt (CAOB). Precambrian Res. 290, 32–48.